IEEE Access
Multidisciplinary : Rapid Review : Open Access Journal

Received November 11, 2020, accepted December 6, 2020, date of publication December 11, 2020, date of current version December 31, 2020.

Digital Object Identifier 10.1109/ACCESS.2020.3044197

An Improved Single-Epoch GNSS/INS Positioning Method for Urban Canyon Environment Based on Real-Time DISB Estimation

FEI YE, SHUGUO PAN, WANG GAO, HAO WANG, GUOLIANG LIU, CHUN MA, AND YUNFENG WANG
School of Instrument Science and Engineering, Southeast University, Nanjing 210096, China

Corresponding author: Shuguo Pan (psg@seu.edu.cn)

This work was supported in part by the National Natural Science Foundation of China under Grant 41774027, and in part by the National Key Technologies Research and Development Program under Grant 2016YFB0502101.

ABSTRACT As one of the commonly used solutions for vehicular dynamic positioning, the stability of Global Navigation Satellite Systems (GNSS)/ Inertial Navigation System (INS) integrated positioning when applied in an urban environment is still struggling. Generally, carrier-phase ambiguity fixing requires continuous several epochs, the stability and continuity of integrated positioning are significantly reduced if the signal is frequently blocked. To reduce the impact of frequent signal blockage, an improved tightly-coupled algorithm is proposed in this paper. Firstly, a step-wise ambiguity processing method is introduced to form instantaneous fixed Wide-Lane (WL) observations for calibrating INS measurement. Secondly, by estimating the differential inter-system bias (DISB) parameter, the pivot satellite can be shared between different constellations, to increase the number of usable satellites under the limited observation conditions and improve the positioning performance. The proposed method is verified with vehicular experiments on semi-simulated and actual urban canyon scenarios. In the artificial GNSS outage experiment, in the situation of 4 satellites that can be observed in BeiDou Navigation Satellite System (BDS) and Global Positioning System (GPS), the positioning accuracy of the proposed algorithm can achieve 4.1cm horizontally and 15.2cm vertically. An improvement of 26.9% horizontally and 20.4% vertically is gained accordingly compared to the conventional method. In the actual urban environment experiment, in case of insufficient satellite and low signal-to-noise ratio (SNR), when the conventional method can no longer maintain a fixed solution of GNSS/INS integrated positioning, the proposed algorithm can still achieve an accuracy of 49.7cm horizontally and 67.0cm vertically.

INDEX TERMS GNSS/INS, urban canyon, DISB, EWL/WL, vehicular positioning.

I. INTRODUCTION

With the development of autonomous driving, vehicular absolute positioning in urban canyons is a hot research topic in recent years. Due to the existence of complex signal blockage, it is hard to get stable high-accuracy positioning in urban canyons only rely on Global Navigation Satellite Systems (GNSS) [1]–[3]. In some heavy interference scenarios, the accuracy of the obtained result is also difficult to break through into meter level. To solve this problem, researchers from various countries have proposed different solutions. For example, visual lane-line identification [4] or behavioral prediction [5] are used as constraints. Those scene constraint methods can constrain the vehicle's position on the driveway, but the disadvantage is that the accuracy still stays at meter level. High-resolution 3D city models can realize high-accuracy positioning [6]. Yet, the building and maintaining of a centimeter-level-model is quite costly. Moreover, positioning results and coordinates in models can't match in real-time [7]. For those reasons, the high-accuracy positioning method based on high-resolution-models stays theoretical. In contrast, the tightly-coupled GNSS and Inertial Navigation System (INS) integration is still the most classic solution to deal with dynamic positioning in complex environments.

Although GNSS measurements can achieve positioning accuracy from meters to centimeters, they are still not sufficient to ensure continuous and accurate positioning

The associate editor coordinating the review of this manuscript and approving it for publication was Erwu Liu.

This work is licensed under a Creative Commons Attribution 4.0 License. For more information, see https://creativecommons.org/licenses/by/4.0/

performance in urban environments [8]. INS can maintain stable positioning without GNSS, while the disadvantage is the positioning performance diverges over time. In the two classical GNSS/INS integration modes, loosely- and tightly-coupled, GNSS measurements are used to limit the INS error accumulation. In between, the loose coupling architecture is integrated based on solutions of respective sensors. The prerequisite of GNSS independently positioning results makes the loosely-coupled integration unsuitable for using in complex signal blockage scenarios. On the contrary, the tightly-coupled integration calibrates INS error divergence with raw GNSS observations. Thus, tight coupling architecture performs better in the complex environment such as urban canyons [9]. To further improve positioning performance in urban areas, velocity and the small changing altitude in cities are using as constraints for maintaining the INS error bounded in the case of GNSS outage [10]. Besides, the multipath mitigation algorithms are implemented to improve the quality of GNSS observations [11]. Researchers also investigated innovative improvements into the fusion algorithms, i.e., the Kalman Filter (KF) and its variants [12]. For example, context-aided framework [13], extreme learning machine [14], and random forest [15], were used to provide high-accuracy positioning solution for an urban environment.

The blocking of Line-of-Sight (LOS) signals and the generating of multipath effects lead to positioning failure in urban areas [16], [17]. For example, the shadow matching technology [18] reduces interference of Non-Line-of-Sight (NLOS) on positioning by matching the predicted and measured satellite visibility. However, insufficient visible satellites caused by severe LOS blockages restricts GNSS observations functioning in the integrated positioning. Normally, INS reckons independently during GNSS outages, but it's hard to maintain stable in commonly happened traffic jams in urban areas. This article aims at further utilizing restricted GNSS signals to improve performance of GNSS/INS integrated positioning in urban environments. Even though the tightly-coupled GNSS/INS integration can calibrate error bias with small visible satellite number, more satellite observations can make the calibration more accurate.

The above situation is appeared in our actual testing. We usually use the classical intra-system differencing (also known as loose combination) model to form double-differenced (DD) observations. However, in the test corresponding to Fig. 1, we found that although the total observable satellite number reached 6 in many epochs, the number of BeiDou Navigation Satellite System (BDS) and Global Positioning System (GPS) are both no more than 3. In the DD mode with such satellite number, for the loosely-coupled GNSS/INS integration, INS is forced to reckon independently because the GNSS positioning is not achievable. Even for tightly-coupled GNSS/INS integrated positioning, the accuracy is affected due to fewer observations. With estimating the differential inter-system bias (DISB) parameter, different constellations can share one global pivot satellite [19], [20]. By taking its stable

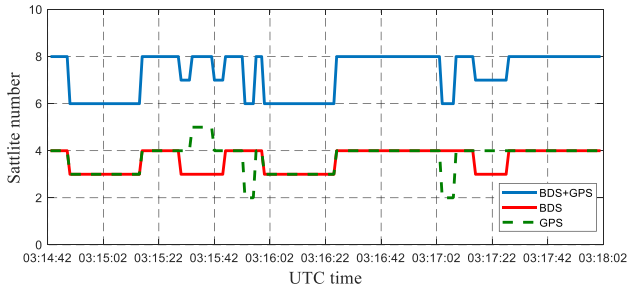

FIGURE 1. The visible satellite numbers in urban canyon simulation.

FIGURE 2. Positioning processed with inter-system differencing algorithm. The yellow dots in box can't obtain results with classical loose combination model.

time-varying characteristic [21], it allows forming differencing across systems. And the resulting redundant observations strengthen the positioning model [22]. That is essential for signal blockage scenarios, e.g., the urban areas [23]. As the key parameter for using the inter-system model, the DISB can be estimated in real-time [24] and used for fixing DD ambiguity into integer [25], [26]. The inter-system model is also verified that it can improve single-epoch Ambiguity Resolution (AR) performance with high cut-off elevation [27], which is exactly matched GNSS signal reception characteristics in urban canyons. In the example mentioned above, the inter-system differencing is used instead of the classical differencing model, the positioning results in Fig. 2 are now obtainable.

In this paper, we introduce two GNSS observation processing techniques to make the tightly-coupled GNSS/INS integration more adaptable to the frequent signal blockage environments. The Extra-wide-lane (EWL)/Wide-lane (WL) stepwise ambiguity resolution supports obtaining the ambiguity fixed GNSS observations in a single epoch. The inter-system differencing allows maximizing the usage of limited observable satellites. Thereby improving the stability of high accuracy tightly-coupled GNSS/INS integrated positioning when applied in a complex urban environment. The contribution is mainly reflected in two aspects: one is the avoidance of the influence on subsequent epoch observations when ambiguity fixing error occurs; the other is the reducing

of computational burden in GNSS/INS integration by not using an addition KF and Least-squares AMBiguity Decorrelation Adjustment (LAMBDA) algorithm when ambiguity resolution. Later in this contribution, the positioning performance with the proposed method and its comparison with a conventional tightly-coupled GNSS/INS integration method is tested using a set of short baseline data collected in a real traffic environment.

The rest of this paper is organized as follows. In Section II, based on the GNSS triple-frequency single-epoch observations and the inter-system differencing model, a tightly-coupled GNSS/INS integration based on the inter-system WL observation is proposed, and the corresponding integration scheme is given. In order to verify the effectiveness and advantages of the proposed method, semi-simulation and actual field experiments are carried out in Section III, together with detailed experimental procedures and results are given. Section IV analyzes the experimental results in detail, and discusses the advantages and disadvantages of the proposed method. The conclusion and future work are given in Section V.

II. METHODS

A. GNSS TRIPLE FREQUENCY SINGLE-EPOCH OBSERVATIONS

For short baseline applications, the triple-frequency observation equations [28] can be expressed as:

$$\Delta\nabla\phi_{(i,j,k)} = \cdot\Delta\nabla\rho+\Delta\nabla T - \eta_{(i,j,k)}\Delta\nabla I + \lambda_{(i,j,k)}\Delta\nabla N_{(i,j,k)}+\Delta\nabla\varepsilon_{(i,j,k)} \quad (1)$$

$$\Delta\nabla P_{(i,j,k)} = \Delta\nabla\rho+\Delta\nabla T - \eta_{(i,j,k)}\Delta\nabla I+\Delta\nabla e_{(i,j,k)} \quad (2)$$

where $\Delta\nabla\phi_{(i,j,k)}$ and $\Delta\nabla P_{(i,j,k)}$ are DD linear combinations of triple-frequency carrier-phase and pseudorange observations, which can be expressed as follows [29]:

$$\Delta\nabla\phi_{(i,j,k)} = \frac{if_1\Delta\nabla\phi_1 + jf_2\Delta\nabla\phi_2 + kf_3\Delta\nabla\phi_3}{if_1 + jf_2 + kf_3} \quad (3)$$

$$\Delta\nabla P_{(\mathrm{i,j,k})} = \frac{if_1\Delta\nabla P_1 + jf_2\Delta\nabla P_2 + kf_3\Delta\nabla P_3}{if_1 + jf_2 + kf_3} \quad (4)$$

where i, j, k are the combination coefficient of triple-frequency carrier-phase, f_1, f_2, f_3 are three frequencies. $\Delta\nabla\phi_1, \Delta\nabla\phi_2, \Delta\nabla\phi_3$ are DD carrier-phase observations in each frequency presented in the unit of meter. $\Delta\nabla P_1, \Delta\nabla P_2, \Delta\nabla P_3$ are DD pseudorange observations of each frequency. In (3) and (4), the linear combination may increase the atmospheric effects even with DD processing [30]. Considering wavelength and noise amplification coefficient, the combination of $(0, -1, 1)$ and $(1, -1, 0)$ are the most suitable for EWL and WL of BDS [31]. On GPS side, $(1, 0, -1)$ has similar effect as $(1, -1, 0)$ for WL combination [32]. However, to maintain the algorithm consistency, we also use $(0, -1, 1)$ for EWL and $(1, -1, 0)$ for WL when processing GPS triple-frequency observations. When the carrier-phase combination coefficient is settled, the carrier-phase noise is minimized by adjusting the pseudorange combination coefficient to (0, 1, 1) [33], [34].

To realize a single epoch ambiguity resolution, the principle is to fix EWL ambiguity first, then use the result to fixing WL ambiguity [32]. The geometry-free and ionospheric-free model (GIF) is used to calculate the ambiguity of EWL. The calculation is expressed as follows:

$$\Delta\nabla N_{(0,-1,1)} = \left[\frac{\Delta\nabla\phi_{(0,-1,1)}-\Delta\nabla P_{(0,1,1)}}{\lambda_{(0,-1,1)}}\right] \quad (5)$$

where $\Delta\nabla N_{(0,-1,1)}$ is the DD ambiguity of EWL with combination of (0,-1,1). $\lambda_{(0,-1,1)}$ is the combined wavelength of triple-frequency. $\Delta\nabla\phi_{(0,-1,1)}$ stands for DD carrier-phase observation accordingly. $\Delta\nabla P_{(0,1,1)}$ represents pseudorange observation of combination (0, 1, 1). Both $\Delta\nabla\phi_{(0,-1,1)}$ and $\Delta\nabla P_{(0,1,1)}$ are in unit of meter. Once the EWL ambiguity solved, the formula for processing WL ambiguity can be built based on Three Carrier Ambiguity Resolution (TCAR) algorithm [35] as follows:

$$\Delta\nabla N_{(1,-1,0)} = \cdot\frac{1}{\lambda_{(1,-1,0)}}\big[\Delta\nabla\phi_{(1,-1,0)} - \Delta\nabla\phi_{(0,-1,1)} - \big(\eta_{(0,-1,1)} - \eta_{(1,-1,0)}\big) \times \Delta\nabla I + \lambda_{(0,-1,1)}\Delta\nabla N_{(0,-1,1)}\big] \quad (6)$$

The troposphere and orbit errors are eliminated [36], leaving only carrier observation noise and ionospheric delay η, the influences of which are controllable. The ionospheric delay (in unit of meter) influence coefficient can be obtained by (7):

$$\frac{\eta_{(0,-1,1)} - \eta_{(1,-1,0)}}{\lambda_{(1,-1,0)}} = -0.352 \quad (7)$$

Since the ionospheric delay has a small influence coefficient, the ionospheric delay can be ignored for short baseline applications. Because of the small atmospheric noise influence and long wavelength, the WL ambiguities can be accurately fixed by rounding to integer.

B. THE INTER-SYSTEM DIFFERENCING MODEL

Taking BDS as the reference system and GPS as the observation system for example. The short baseline DD observation equation can be expressed as (8):

$$\nabla\Delta\varphi^{1_CS} = \cdot\nabla\Delta\rho^{1_CS} + \lambda^G\Delta N^S - \lambda^C\Delta N^{1_C} + \lambda^G\delta^{CG} + \nabla\Delta T^{1_CS} + \nabla\Delta\varepsilon^{1_CS} \quad (8)$$

where Δ is single difference operator, which means single difference between stations. $\nabla\Delta$ is the DD operator. φ is the carrier-phase observation, ρ is satellite-station distance, λ represents wavelength, N is the ambiguity, and ε represents observation noise. The letter C and G in superscript represents for the system of BDS and GPS. The parameter δ^{CG} is used here to represent the hardware phase delay between BDS and GPS [37]. We use 1_C to represent the BDS reference satellite. Similarly, in the following text, 1_G will be used to indicate GPS reference satellite. We also use S to represent visible satellite of GPS. In the case of short baseline, the clock bias and ionospheric error parameters are considered to be

eliminated. But the tropospheric error still cannot be ignored for baselines above 15km, which is represented by T in (8). Because wavelength is different between two systems, the parameters with wavelength can't be processed directly yet. The ambiguity parameters are adjusted as follows:

$$\begin{aligned}\lambda^G\Delta N^S - \lambda^C\Delta N^{1C} &= \cdot\lambda^G\Delta N^S - \lambda^G\Delta N^{1C} + \lambda^G\Delta N^{1C}\\ -\lambda^C\Delta N^{1C} &= \lambda^G\nabla\Delta N^{1CS} + \left(\lambda^G - \lambda^C\right)\Delta N^{1C}\end{aligned} \tag{9}$$

where $\nabla\Delta N^{1CS}$ can be further transformed to:

$$\begin{aligned}\nabla\Delta N^{1CS} &= \Delta N^S - \Delta N^{1C} = \Delta N^S - \Delta N^{1G} + \Delta N^{1G}\\ -\Delta N^{1C} &= \nabla\Delta N^{1GS} + \nabla\Delta N^{1C1G}\end{aligned} \tag{10}$$

Therefore, the DD observation equation as (8) can be transformed into:

$$\begin{aligned}&\nabla\Delta\varphi^{1CS}\\ &= \cdot\nabla\Delta\rho^{1CS} + \lambda^G\nabla\Delta N^{1C1G} - \lambda^C\Delta N^{1C} + \lambda^G\delta^{CG}\\ &\quad +\lambda^G\nabla\Delta N^{1GS} + \nabla\Delta T^{1CS} + \nabla\Delta\varepsilon^{1CS}\\ &= \cdot\nabla\Delta\rho^{1CS} + \lambda^G\left[\nabla\Delta N^{1C1G} + \left(1 - \frac{\lambda^C}{\lambda^G}\right)\right.\\ &\quad \left.\cdot\Delta N^{1C} + \delta^{CG}\right] + \lambda^G\nabla\Delta N^{1GS} + \nabla\Delta T^{1CS} + \nabla\Delta\varepsilon^{1CS}\end{aligned} \tag{11}$$

Furthermore, let $\bar{\delta}^{CG} = \nabla\Delta N^{1C1G} + \left(1 - \frac{\lambda^C}{\lambda^G}\right)\Delta N^{1C} + \delta^{CG}$, (11) can be changed to:

$$\begin{aligned}\nabla\Delta\varphi^{1CS} = \cdot\nabla\Delta\rho^{1CS} + \lambda^G\bar{\delta}^{CG} + \lambda^G\nabla\Delta N^{1GS} + \nabla\Delta T^{1CS}\\ + \nabla\Delta\varepsilon^{1CS}\end{aligned} \tag{12}$$

where $\bar{\delta}^{CG}$ is the DISB parameter needs to be estimated. The inter-system model of BDS and GPS with WL observation can be expressed as follows:

$$\begin{aligned}\nabla\Delta\varphi_{WL}^{1CS} = \cdot\nabla\Delta\rho_{WL}^{1CS} + \lambda_{WL}^G\left(\bar{\delta}_{WL}^{CG} + \nabla\Delta N_{WL}^{1GS}\right)\\ +\nabla\Delta T_{WL}^{1CS} + \nabla\Delta\varepsilon_{WL}^{1CS}\end{aligned} \tag{13}$$

C. TIGHTLY-COUPLED GNSS/INS INTEGRATION MODEL WITH INTER-SYSTEM WL OBSERVATION

The state vector of classical tightly-coupled GNSS/INS integration is designed based on INS error. The state vector difference between the proposed algorithm and the traditional design is the DISB parameter. Therefore, the state vector is a 16-dimensional vector as follows:

$$X = \left[\, dr_{3\times1}\ dv_{3\times1}\ d\theta_{3\times1}\ \nabla_{3\times1}\ a_{3\times1}\ \bar{\delta}_{WL}^{CG}\,\right]^T \tag{14}$$

where X is the state vector, dr, dv and $d\theta$ are presenting the positioning, velocity, and attitude error vectors . The three vectors are normally expressed with symbol δ. Here the use of symbol d is to distinguish with DISB parameter $\bar{\delta}_{WL}^{CG}$. Other symbols such as ∇ is the gyro bias error vector, a is the accelerometer bias error vector. The DISB is relative independent between epochs, its value is mainly affected by the satellite ambiguity of the current epoch. Therefore, the transfer coefficient of DISB is 1 in the system matrix of the state model. On the other hand, the measurement equation of GNSS/INS tightly-coupled model with inter-system WL observation can be expressed as follows:

$$\begin{aligned}&\nabla\Delta\varphi_{WL}^{1CS} - \nabla\Delta\varphi_{INS}^{1CS}\\ &= \cdot\left(\nabla\Delta\rho_{WL}^{1CS} - \nabla\Delta\rho_{INS}^{1CS}\right)\\ &\quad +\lambda_{WL}^G\left(\bar{\delta}_{WL}^{CG} + \nabla\Delta N_{WL}^{1GS}\right) + \nabla\Delta T_{WL}^{1CS} + \nabla\Delta\varepsilon_{WL}^{1CS}\end{aligned} \tag{15}$$

where $\nabla\Delta\varphi_{INS}^{1CS}$ and $\nabla\Delta\rho_{INS}^{1CS}$ are the DD inter-system carrier-phase observations and geometry distance inferred from INS observations. This equation described the measurement error between GNSS and INS. Because $\nabla\Delta N_{WL}^{1GS}$ and $\nabla\Delta T_{WL}^{1CS}$ can be precisely calculated, after further transformation, (15) can be changed to:

$$\begin{aligned}&\left(\nabla\Delta\varphi_{WL}^{1CS} - \lambda_{WL}^G\nabla\Delta N_{WL}^{1GS} - \nabla\Delta T_{WL}^{1CS}\right) - \nabla\Delta\varphi_{INS}^{1CS}\\ &= \nabla\Delta e_1^{1CS}dx + \nabla\Delta e_2^{1CS}dy + \nabla\Delta e_3^{1CS}dz + \lambda_{WL}^G\bar{\delta}_{WL}^{CG}\\ &\quad + \nabla\Delta\varepsilon_{WL}^{1CS}\end{aligned} \tag{16}$$

where $\nabla\Delta e_1^{1CS}$, $\nabla\Delta e_2^{1CS}$, $\nabla\Delta e_3^{1CS}$ represents direction cosine, dx, dy, dz are the positioning errors. Let $\nabla\Delta\bar{\varphi}_{WL}^{1CS} = \nabla\Delta\varphi_{WL}^{1CS} - \lambda_{WL}^G\nabla\Delta N_{WL}^{1GS} - \nabla\Delta T_{WL}^{1CS}$, the measurement equation of kth. epoch can be expressed as:

$$\begin{aligned}&\nabla\Delta\bar{\varphi}_{WL,k}^{1CS} - \nabla\Delta\varphi_{INS,k}^{1CS}\\ &= \cdot\nabla\Delta e_{1,k}^{1CS}dx + \nabla\Delta e_{2,k}^{1CS}dy + \nabla\Delta e_{3,k}^{1CS}dz + \lambda_{WL}^G\bar{\delta}_{WL,k}^{CG}\\ &\quad + \nabla\Delta\varepsilon_{WL,k}^{1CS}\end{aligned} \tag{17}$$

Rewrite (17) into matrix mode, the measurement model improved with inter-GNSS estimation and EWL/WL observations is proposed as follows (18), as shown at the bottom of the next page:

The stochastic model used in this research is based on GNSS observation noise. Use symbol R for presenting the undifferenced phase and code covariance matrix, and R_d for the double-differenced version. The matrix R is formed based on observation noise experience value (0.005m for phase and 0.5m for code observations), then weighted with elevation function and differenced operator. With the double-differenced transformation matrix T_d, we can have the observation stochastic model as follows:

$$R_d = T_d R T_d^T \tag{19}$$

Besides, the system noise covariance matrix is based on the IMU error with white noise. The error corresponding to the carrier-phase DISB parameter is set according to the expected deviation of 0.05 cycles per hour.

D. INTEGRATION SCHEME

With the conventional method, for the use of carrier-phase observation, a Kalman Filter and then LAMBDA algorithm are necessary for AR. On one hand, frequent signal blockage

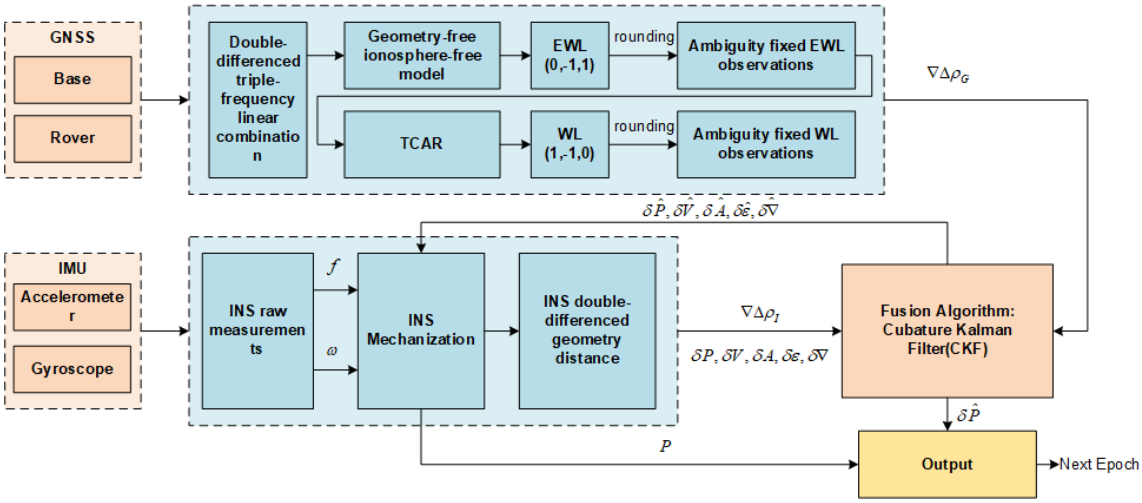

FIGURE 3. The proposed integration scheme.

FIGURE 4. Measurement vehicle for testing.

is easy to cause instable and unreliable of the multi-epoch AR during the GNSS update processing. On the other hand, double Kalman Filters (one for AR estimating and the other for GNSS/INS fusion) significantly increase the complexity of integration. We introduced triple-frequency observations and the corresponding process method for obtaining GNSS measurements. The introduced process is a single-epoch calculation, much easier than using an estimation algorithm, so that it can reduce the complexity of the integration scheme.

In Fig. 3, P, f, ω are the raw measurements of INS sensors, which stands for the position, specific force and angle velocity obtained from accelerometer and gyroscope; $\delta P, \delta V, \delta A, \delta\varepsilon, \delta\nabla$ referred to the state from INS of the current epoch, as the input of fusion algorithm; $\delta\hat{P}, \delta\hat{V}, \delta\hat{A}, \delta\hat{\varepsilon}, \delta\hat{\nabla}$ stand for the estimated state vector outputted by fusion algorithm, which are going to be used for the next epoch as input; $\Delta\nabla\rho_G$ and $\Delta\nabla\rho_I$ are measurements of GNSS and INS, which are using for consisting measurement vectors. The fusion algorithm in this paper is the standard Cubature Kalman Filter (CKF). CKF is the most efficient fusion algorithm in the latest integrated navigation and positioning research. The estimation process of standard CKF [38] is not going to be explained in this article.

III. RESULTS

A. EXPERIMENT SETUP

1) HARDWARE SETUP

A measurement vehicle (Fig. 4) assembled NovAtel SPAN-ISA-100C INS (0.5°/h gyro) with a PP6 GNSS receiver (Fig. 5) was carried out as the benchmark system for evaluating the performance of the proposed algorithm. Besides, a GNSS receiver T300 from ComNav, which could receive BDS and GPS triple-frequency observations, is used to build the testing system. The benchmark and testing systems are deployed in zero-baseline mode. Signal is transmitting to both systems through the same antenna and a splitter, to ensure distance deviation is excluded during the dynamic evaluation (Fig. 6).

The specific parameters of IMU that we used in the experiment are listed in Table 1.

$$\begin{bmatrix} \nabla\Delta\bar{\varphi}^{1_CS_1}_{WL,k} - \nabla\Delta\varphi^{1_CS_1}_{INS,k} \\ \nabla\Delta\bar{\varphi}^{1_CS_2}_{WL,k} - \nabla\Delta\varphi^{1_CS_2}_{INS,k} \\ \vdots \\ \nabla\Delta\bar{\varphi}^{1_CS_j}_{WL,k} - \nabla\Delta\varphi^{1_CS_j}_{INS,k} \end{bmatrix} = \cdot \begin{bmatrix} \nabla\Delta e^{1_CS_1}_{1,k} & \nabla\Delta e^{1_CS_1}_{2,k} & \nabla\Delta e^{1_CS_1}_{3,k} & 0_{1\times 12} & \lambda^G_{WL} \\ \nabla\Delta e^{1_CS_2}_{1,k} & \nabla\Delta e^{1_CS_2}_{1,k} & \nabla\Delta e^{1_CS_2}_{1,k} & 0_{1\times 12} & \lambda^G_{WL} \\ \vdots & \vdots & \vdots & \vdots & \vdots \\ \nabla\Delta e^{1_CS_j}_{1,k} & \nabla\Delta e^{1_CS_j}_{1,k} & \nabla\Delta e^{1_CS_j}_{1,k} & 0_{1\times 12} & \lambda^G_{WL} \end{bmatrix} \cdot \begin{bmatrix} \delta r_{3\times 1} \\ \delta v_{3\times 1} \\ \delta\theta_{3\times 1} \\ \nabla_{3\times 1} \\ a_{3\times 1} \\ \bar{\delta}^{CG}_{WL,k} \end{bmatrix} + \begin{bmatrix} \nabla\Delta\varepsilon^{1_CS_1}_{WL,k} \\ \nabla\Delta\varepsilon^{1_CS_2}_{WL,k} \\ \vdots \\ \nabla\Delta\varepsilon^{1_CS_j}_{WL,k} \end{bmatrix} \quad (18)$$

FIGURE 5. NovAtel SPAN-ISA-100C System.

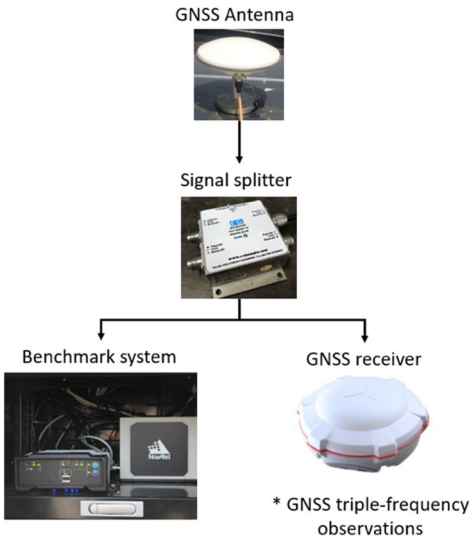

FIGURE 6. Zero-baseline reception schematic.

TABLE 1. NovAtel ISA-100C IMU specifications.

Items	Gyroscope	Accelerometer
Bias stability	0.5deg/h	100μg
Scale factor	100ppm	1250μg
Random walk	0.012 deg/ √ hr	100μg/√hr
Linearity	100ppm	100ppm
Data rate	200Hz	

2) TEST FLOW

We collected BDS and GPS observations to test the performance of the proposed algorithm. A reference station and the measurement vehicle were forming a pair of station-difference. An offline process software Waypoint Inertial Explorer (IE) was used for processing high-accuracy positioning results. The millimeter level result is used as ground truth during the experiments. More than 1000 epochs short baseline differenced data were involved in calculation. Those epochs in the period but without complete triple-frequency BDS observations did not participate. The driving trajectory is as shown in Fig. 9.

Since the GNSS positioning technique based on triple-frequency WL observations can realize single-epoch high-accuracy positioning in a complex environment, the experiment was performed based on this technique to verify the positioning ability of the proposed algorithm in urban canyon. The core difference between the proposed and the conventional algorithms was the different use of GNSS observations. Although pseudorange is also single epoch observation, the accuracy was insufficient. Although the accuracy of the Narrow-lane (NL) carrier observation is high, the ambiguity is frequently re-fixed in a complex environment, which seriously affects its stability. The triple-frequency WL combination observation based on the classic differencing is fixing ambiguity in single epoch while ensuring a high accuracy. In order to effectively compare the positioning performance, the comparison algorithm used in this paper is based on wide-lane single epoch observations, which is called the conventional algorithm in the rest of this paper. We compare the proposed algorithm (with the inter-system differencing model) and the conventional algorithm (with the classic intra-system differencing model) with the same data in the experiments.

3) URBAN CANYON SIMULATION

Because it's hard to find a representative urban canyon environment in the local area of Nanjing, China. The simulated urban canyon is used instead by excluding part of the visible satellite signals. Different strategies of satellite number controlling are used to ensure that three possible situations may occur in the actual traffic environment. The three situations are:

- The number of visible satellites is seriously insufficient, BDS has less than 4 visible satellites and GPS has only 1 satellite observable;
- The number of visible satellites is still small, a total of more than 5 visible satellites can be reached by two systems;
- Set no limitation to receive the satellite signal, so that the sufficient satellite numbers are ensured. The experiment will focus on the performance of the proposed algorithm in these three scenarios, and the positioning accuracy is set as the main evaluation parameter.

The characteristic of satellite visibility in urban areas is the satellites along the longitudinal axis of streets are visible, while those on the axis going across the street are affected by the buildings aside. In other words, signals going across the street in an urban canyon will be mostly blocked while the signals going along the street not [39], [40]. Therefore, the realization of the simulation environment is mainly achieved by restriction of the observation angle, i.e., the elevation and azimuth. The schematic of setting up elevation and azimuth mask angle are shown in Fig. 7.

Consider the vehicle driving on a street, the direction of the street is obtained by the heading angle of INS output. On the horizontal plane along the longitudinal axis of streets, we set up a pair of fan-shaped areas in front and rear direction

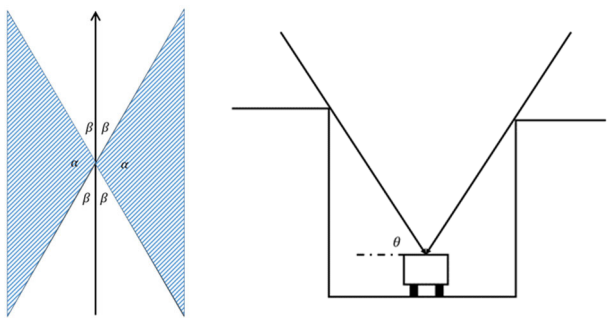

(a) (b)

FIGURE 7. Elevation and azimuth mask in urban canyon. (a) Azimuth angle blockage. (b) Elevation angle blockage.

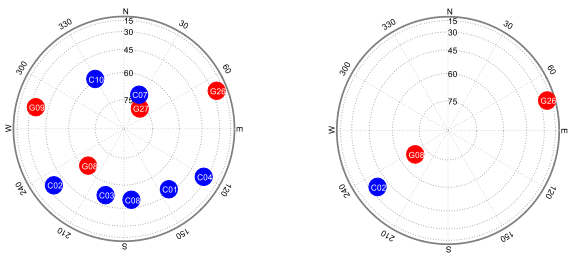

(a) (b)

FIGURE 8. Sky plot of one single epoch. (a) Before simulating. (b) After simulating.

with a central angle of 30 degrees, as non-blocking areas. The satellite elevation mask angle in the non-blocking area is set as usual. Those in blocking areas are set at a high angle. As shown in Fig. 7(a), the direction indicated by the arrow is the direction of driving, and the angle between driving direction and true north can be expressed by the heading angle γ. Using β to represent the angle between driving direction and longitudinal blockage, and α for the open-angle of the sector-area that representing the building shielding area. Assume $\alpha \in [0,360^\circ]$ and clockwise for positive direction, the determination of angle α follows (20):

$$\alpha \in \begin{cases} [\gamma+\beta, \gamma+180^\circ-\beta] \cup [\gamma+\beta, \gamma+180^\circ-\beta], \\ \qquad \gamma \le 180^\circ \\ [0, \gamma-180^\circ-\beta] \cup [\gamma+\beta, 360^\circ] \\ \qquad \cup [\gamma-180^\circ+\beta, \gamma-\beta], \quad \gamma > 180^\circ \end{cases} \tag{20}$$

In the sector area, the side blocking raises the elevation cutoff. In Fig. 7(b) we use θ to represent the elevation mask. In this paper we assume that 75 degrees is appropriate as the lowest elevation angle in the side blocking sector of urban canyon. The sky plot of one epoch is shown as an example of satellite observation simulation of urban canyons (Fig. 8).

B. EXPERIMENTAL RESULTS

1) METHOD VALIDATION WITH SIMULATED URBAN CANYON

To show the testing environment, different colors are used in Fig. 9 to represent the sections where the simulated GNSS

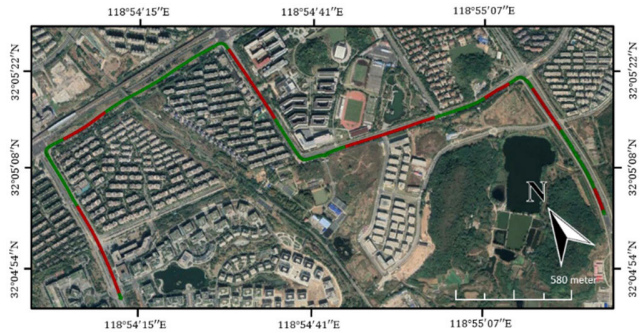

FIGURE 9. Simulating urban canyon sections by limiting visible satellites (green dots means no limitation on visible satellites; red dots are the simulated urban canyon sections).

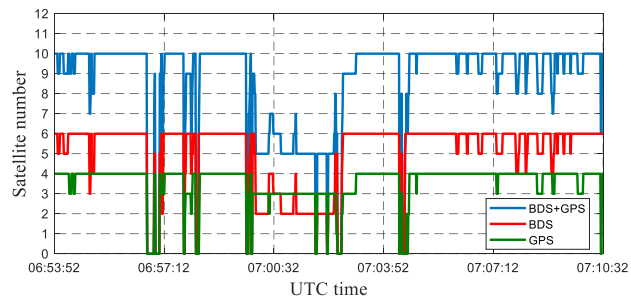

FIGURE 10. Visible Satellite Number in the urban canyon simulation experiment.

TABLE 2. Positioning accuracy with proposed algorithm (*cm*).

Direction	RMS
E	11.2
N	8.3
U	27.2
Horizontal	14.0
Overall	30.6

outages are implemented. The related visible satellite numbers are presenting in Fig. 10. Fig. 11 shows the error curve of all epochs, which using the proposed GNSS/INS integrated positioning algorithm. The statistical positioning accuracy is indicated in Table 2. Fig. 12-13 are showing the 95% empirical confidence region of horizontal and up direction.

2) THE POSITIONING PERFORMANCE EVALUATION WITH SIMULATED URBAN CANYON

We also compared the positioning performance of the two algorithms through the strategy of limiting visible satellite number in the whole process. The number of visible satellites in the entire section was shielded sequentially by elevation angle. Table 2 and 3 present the statistical accuracy of the conventional and proposed tightly-coupled GNSS/INS integrated positioning algorithm along with visible satellite numbers.

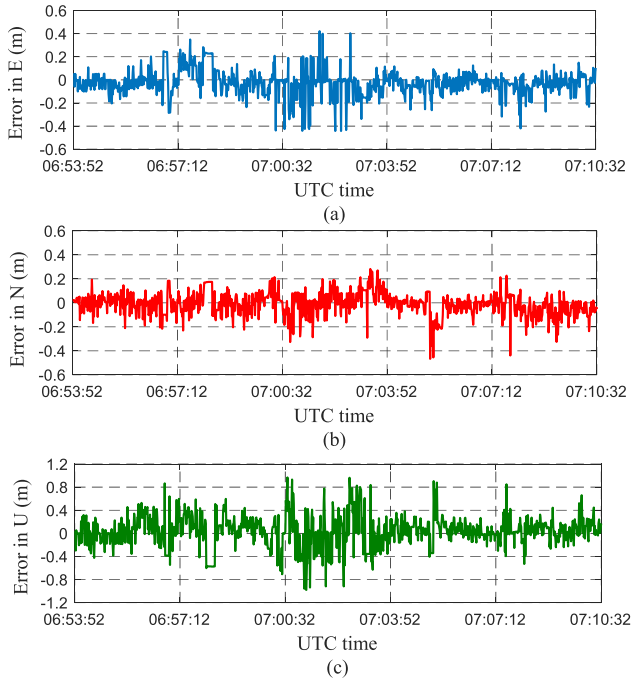

FIGURE 11. Positioning error with inter-system differencing algorithm (*m*). (a) Error in E direction; (b) Error in N direction; (c) Error in U direction.

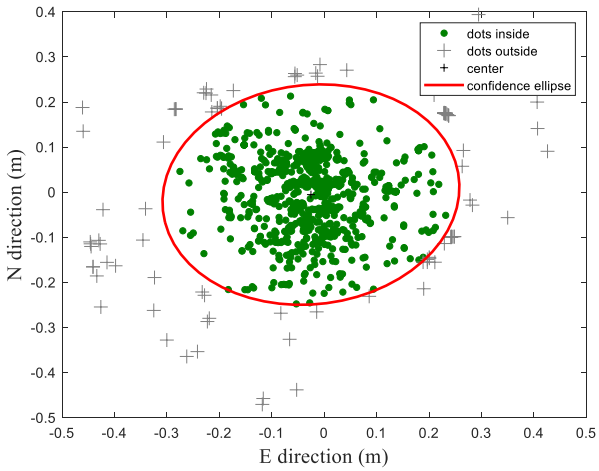

FIGURE 12. The 95% empirical confidence ellipses for Horizontal (N, E) position scatter.

Fig. 14-16 are used for helping present the improvement trend of positioning performance resulted from Table 3 and 4.

The proposed algorithm is compared with the algorithm based on the EWL/WL single epoch observations. No matter the conventional or the proposed method, the positioning accuracy is going higher as the number of satellites increases (Fig. 14 and 15). However, the benefit from method improvement is inverse with more satellite observed (Fig. 16). Take the scenario of 4 satellites observable as an example, 2 BDS and 2 GPS satellites were involved most of the time (Fig. 17), Fig. 18 and 19 present the positioning error curves obtained by the two algorithms.

TABLE 3. Positioning accuracy comparison of the two algorithms (ENU).

Visible satellite number	RMS of positioning errors (*cm*)						Improvement (%)		
	Conventional algorithm			Proposed algorithm					
	E	N	U	E	N	U	E	N	U
4	4.5	3.4	19.1	3.2	2.6	15.2	30.2%	24.5%	20.4%
5	3.8	2.8	15.0	2.8	2.3	12.3	26.5%	19.1%	18.0%
6	3.2	2.7	9.7	2.7	2.1	8.1	16.2%	17.4%	16.2%
7	2.9	2.5	7.9	2.5	2.2	6.7	14.0%	12.0%	15.9%
8	2.4	2.4	6.9	2.2	2.1	6.1	9.1%	5.7%	11.1%
9	2.3	2.1	6.6	2.1	2.0	5.9	7.0%	3.3%	10.8%
10	2.1	2.0	5.6	2.0	2.0	5.0	4.3%	2.0%	9.5%
11	2.1	2.0	5.2	2.0	2.0	4.8	3.8%	1.5%	7.8%

TABLE 4. Positioning accuracy comparison of the two algorithms (Horizontal and overall).

Visible satellite number	RMS of positioning errors (*cm*)				Improvement (%)	
	Conventional algorithm		Proposed algorithm			
	Horizontal	Overall	Horizontal	Overall	Horizontal	Overall
4	5.6	44.1	4.1	39.2	26.9%	11.0%
5	4.6	39.0	3.6	35.3	21.9%	9.6%
6	4.2	31.4	3.5	28.7	16.8%	8.8%
7	3.8	28.4	3.3	26.1	13.0%	8.0%
8	3.3	26.5	3.0	24.9	8.5%	6.0%
9	3.1	25.9	2.9	24.5	6.9%	5.5%
10	2.9	23.8	2.8	22.5	4.9%	5.5%
11	2.9	23.0	2.8	22.1	4.9%	3.9%

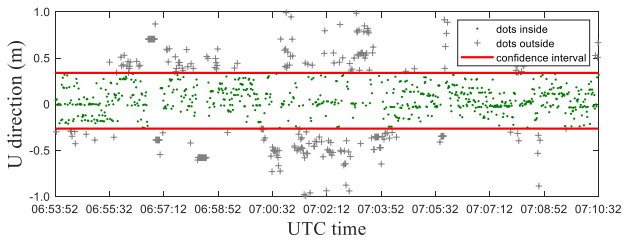

FIGURE 13. The 95% empirical confidence intervals for vertical (U) position scatter.

3) THE ACTUAL TEST IN REAL URBAN ENVIRONMENT

After verifying the performance with the simulated canyon, we also applied the proposed method in the real canyon. The test was carried out in the urban area of Nanjing, China. In this section of the street, the GNSS signals were most severely blocked by obstacles such as sidewalk trees and high-rise buildings on both sides (Fig. 20), resulting in an obvious blockage of the visible satellites (Fig. 21). The visible satellite numbers were mostly only 4 or 5 with frequent blockages. Many of the corresponding signal-to-noise ratio (SNR) are significantly low (Fig. 22). Under this condition, the actual positioning error obtained using the proposed method is shown in Fig. 24, and the statistical accuracy RMS is shown in Table 5.

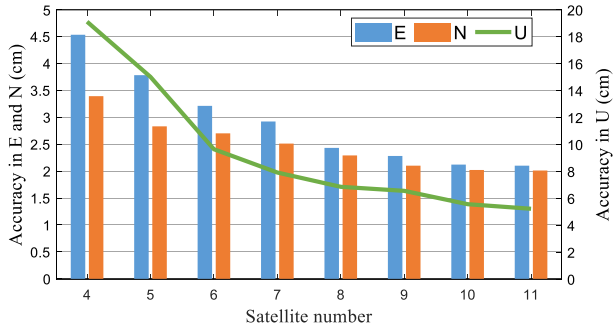

FIGURE 14. Positioning accuracy RMS (*cm*) with the conventional algorithm.

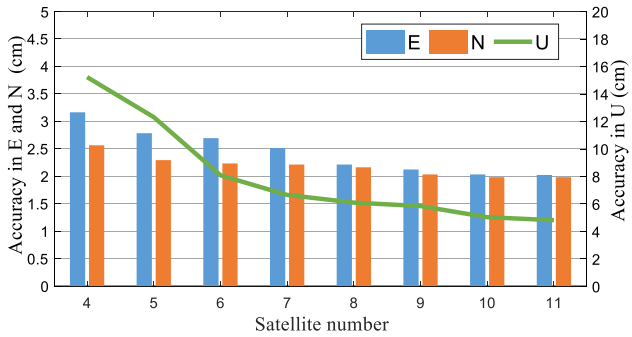

FIGURE 15. Positioning accuracy RMS (*cm*) with the proposed algorithm.

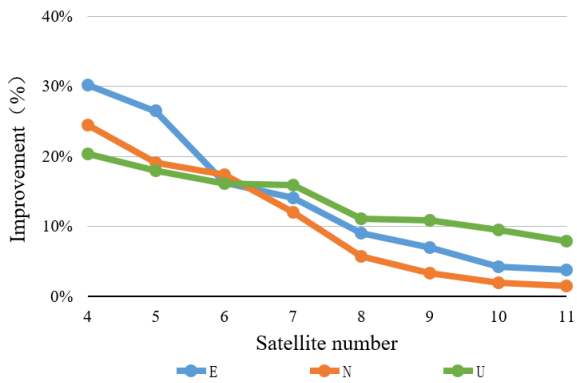

FIGURE 16. Improvement of positioning accuracy along with satellite number.

It can be seen from the sky plot (Fig. 23) that the satellite blockage was mainly from the across-street directions (east and west), while the non-blocking directions were along the street (north and south). Therefore, in the final positioning result, the accuracy of the east direction will be better than the north direction.

IV. DISCUSSION

The first set of experiment verifies that the proposed algorithm appeared under different signal blocking conditions by simulating urban canyons. In this scenario, there are about 70% of the epochs are with sufficient satellite observable,

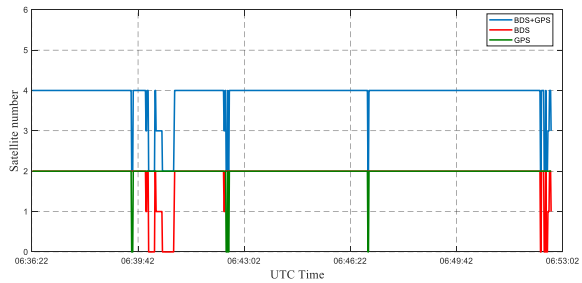

FIGURE 17. The visible satellite number in performance comparison experiment.

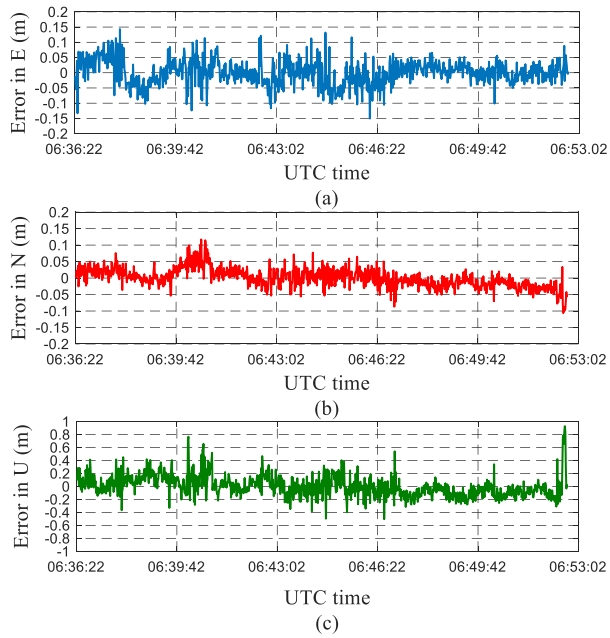

FIGURE 18. Positioning error with the conventional algorithm (*m*). (a) Error in E direction; (b) Error in N direction; (c) Error in U direction.

TABLE 5. Positioning accuracy of the urban environment test (*cm*).

Direction	RMS
E	20.9
N	45.1
U	67.0
Horizontal	49.7
Overall	83.5

20% with medium blockage, and 10% with satellites barely observable. The experimental results indicate an RMS accuracy of 14*cm* for horizontal and 27.2*cm* for vertical, which demonstrate that the proposed algorithm has decimeter level positioning capability in an entire complex environment.

The second experiment is about performance evaluation between the conventional and proposed algorithms. It can

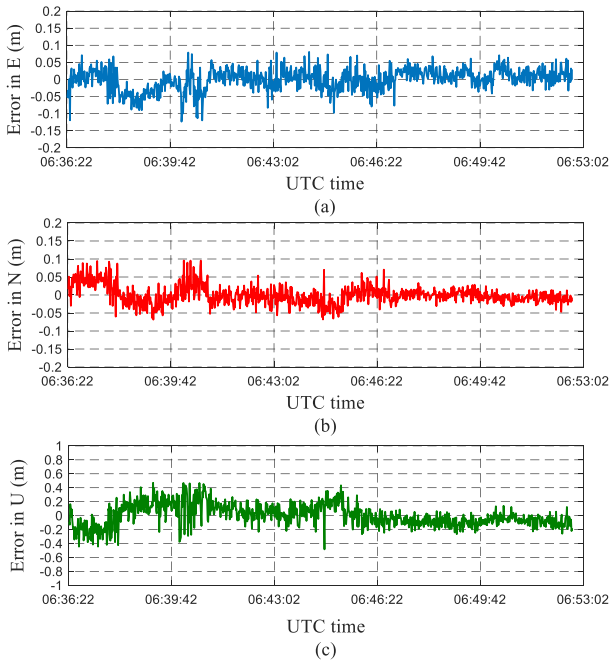

FIGURE 19. Positioning error with the proposed algorithm (*m*). (a) Error in E direction; (b) Error in N direction; (c) Error in U direction.

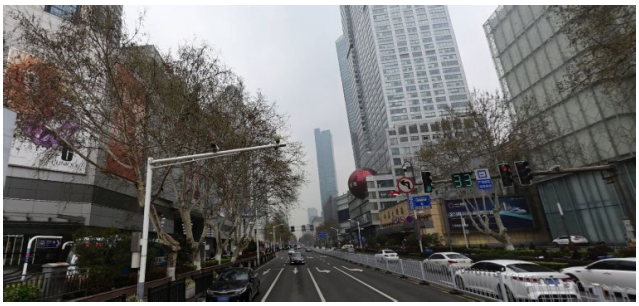

FIGURE 20. The urban environment testing scenario.

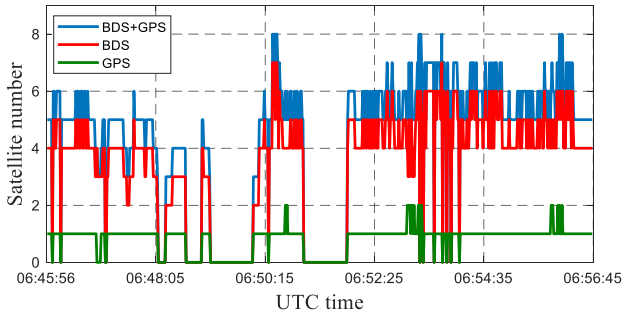

FIGURE 21. The visible satellite number in the urban environment test.

be clearly seen that the curve in Fig. 19 shows a smaller fluctuation than the curve in Fig. 18, i.e., the proposed method is maintaining positioning stability better than the conventional method. Table 2 and 3 indicates that, when the satellite number is blocked to less than 8, the positioning accuracy

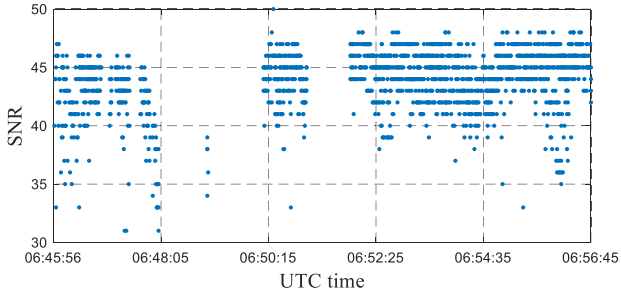

FIGURE 22. The SNR of observations in the urban environment test.

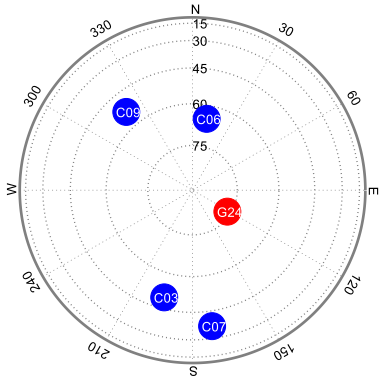

FIGURE 23. The sky plot of visible satellite in the urban environment test.

achieves 3-4*cm* in horizontal and 6*cm* in vertical with more than 20% improvement. Especially, the proposed algorithm is contributing 26.9% for horizontal and 20.4% for vertical improvement of positioning accuracy in the case of 4 visible satellites. When the GNSS signal is heavily blocked, the proposed algorithm does improve the positioning accuracy of tightly-coupled GNSS/INS integration. In contrast, the proposed method can indeed be used in this extreme environment. In the severely blocked epochs, the only GPS satellite is effectively utilized with the inter-system differencing model. For those epochs that satellite signals were frequently blocked, the single-epoch ambiguity fixation guaranteed the GNSS observation stability and continuity. Finally, the statistical positioning accuracy obtained in real urban canyon is 49.7*cm* horizontally and 67.0*cm* vertically. The accuracy meets the expected decimeter-level positioning performance.

The semi-simulated dataset successfully reflects the signal blockage, but still doesn't contain the low SNR characteristics commonly found in real urban canyons. With the actual urban canyon dataset used in the 3rd experiment, the frequent appeared low satellite number and SNR lead to a difficulty of ambiguity fixing with conventional method even if the observation condition was temporarily restored. In which case the positioning relies on INS reckoning while not the GNSS/INS integration. In contrast, the proposed method can indeed be used in this extreme environment. In the severely blocked epochs, the only GPS satellite is effectively utilized with the inter-system differencing model. For

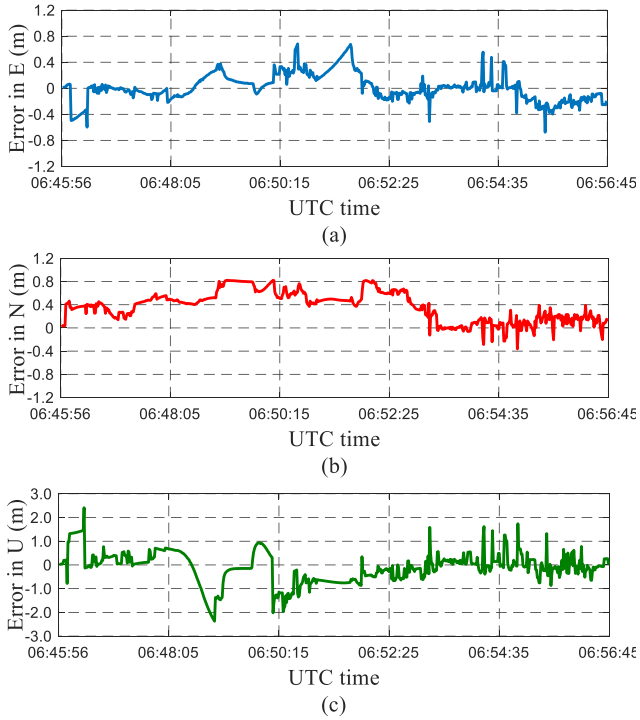

FIGURE 24. Positioning error curve of the urban environment test (*m*). (a) Error in E direction; (b) Error in N direction; (c) Error in U direction.

those epochs that satellite signals were frequently blocked, the single-epoch ambiguity fixation guaranteed the GNSS observation stability and continuity. Finally, the statistical positioning accuracy obtained in real urban canyon is 49.7*cm* horizontally and 67.0*cm* vertically. The accuracy meets the expected decimeter-level positioning performance.

From the above experiments, the proposed method effects better in poor observation environments. Even there is only one satellite observed in one of the systems, the introduced GNSS inter-system differencing model still has the ability to form a redundant observation. By taking advantage of the slow time-varying characteristic of the deviations between systems, the strength of the positioning model is improved, thereby achieving the purpose of improving accuracy (Table 2, about 15%∼20%). However, with sufficient visible satellites, e.g. more than 8 in our case, the positioning accuracy is comparable with the conventional method using an intra-system differencing model (below 10%). In other words, the use of inter-system differencing model helps tightly-coupled GNSS/INS integrated positioning improving accuracy significantly when the visible satellite number is low. Meanwhile, the continued use of the model with sufficient satellites ensures the uniformity of the algorithm without losing accuracy. In addition, the EWL/WL single epoch ambiguity fixing allowed to omit the classic ambiguity searching process, and the dimension of the parameters is greatly reduced, so does the computational pressure.

Due to the larger noise of WL observations, the positioning accuracy of the method we proposed is not as high as that of RTK based on NL observations. The experimental results indicate that a (sub) decimeter level is achieved. Another disadvantage is that the carrier-phase DISB parameter participates in the state vector for estimation. However, only one additional parameter will not bring computational pressure to the original 15-dimensional model.

V. CONCLUSION

This paper contributes to an improved tightly-coupled GNSS/INS positioning method specifically for the urban environment. Due to the frequent signal blockage, the reliability of GNSS carrier-phase observations is decreased, which is further affect the positioning stability of tightly-coupled integration. In order to solve this problem, we used the step-wise ambiguity fixation technology with triple-frequency EWL/WL observations to instantly obtain fixed carrier-phase observations. Then the inter-system differencing technology is implemented to increase the usable satellites under extreme masking situations and further reduce the negative impact of positioning. Based on this, even the DISB parameter increases dimension to the state vector, the entire positioning model greatly reduces the dimension and computational cost due to the simplification of the ambiguity fixing process.

To verify the performance of the proposed algorithm under different signal blockage scenarios, we artificially eliminated observations by different elevation and heading angles based on regular vehicular data. The experimental results on the semi-simulated dataset mainly reveal two conclusions. The first is that the proposed method can indeed achieve decimeter-level positioning results in frequent signal blockage scenarios. Even when only 4 satellites (including GPS and BDS) observable, the positioning accuracy can achieve 4.1*cm* in horizontal and 15.2*cm* in vertical. The second conclusion is that as the number of visible satellites decreases, the improvement has been increased from 4.9% in horizontally and 7.8% vertically of 11 satellites to 26.9% horizontally and 20.4% vertically of 4 satellites. In the actual urban canyon experiment, the positioning result is affected by low signal quality in addition to signal blockage interference. Nevertheless, the proposed algorithm can still achieve a positioning accuracy of 49.7*cm* horizontally and 67.0*cm* vertically, while the conventional method cannot realize integrated positioning due to low signal quality. Take advantage of instant ambiguity fixing and inter-system differencing technology, the proposed method is proven to effectively improve the stability of tightly-coupled GNSS/INS integrated positioning in urban canyons.

After this literature on improving GNSS/INS integration applied in urban canyons, our future work includes the development of an alternative method to detect environmental features based on computer vision to help further restrain positioning errors. Under the premise of GNSS/INS/Vision to achieve higher positioning reliability, autonomous vehicles can further reduce the requirement of auxiliary environmental sensors.

REFERENCES

[1] Y. Cui and S. Sam Ge, "Autonomous vehicle positioning with GPS in urban canyon environments," *IEEE Trans. Robot. Autom.*, vol. 19, no. 1, pp. 15–25, Feb. 2003.

[2] B. Ben-Moshe, E. Elkin, H. Levi, and A. Weissman, "Improving accuracy of GNSS devices in urban canyons," in *Proc. Can. Conf. Comput. Geometry*, 2011, pp. 511–515.

[3] A. Fernandez, M. Wis, P. F. Silva, I. Colomina, E. Pares, F. Dovis, K. Ali, P. Friess, and J. Lindenberger, "GNSS/INS/LiDAR integration in urban environment: Algorithm description and results from ATENEA test campaign," in *Proc. 6th ESA Workshop Satell. Navigat. Technol. (Navitec) Eur. Workshop GNSS Signals Signal Process.*, Dec. 2012, pp. 1–8.

[4] K. Shunsuke, G. Yanlei, and L.-T. Hsu, "GNSS/INS/On-board camera integration for vehicle self-localization in urban canyon," in *Proc. IEEE 18th Int. Conf. Intell. Transp. Syst.*, Sep. 2015, pp. 2533–2538.

[5] B.-H. Lee, J.-H. Song, J.-H. Im, S.-H. Im, M.-B. Heo, and G.-I. Jee, "GPS/DR error estimation for autonomous vehicle localization," *Sensors*, vol. 15, no. 8, pp. 20779–20798, Aug. 2015.

[6] P. Jende, F. Nex, M. Gerke, and G. Vosselman, "A fully automatic approach to register mobile mapping and airborne imagery to support the correction of platform trajectories in GNSS-denied urban areas," *ISPRS J. Photogramm. Remote Sens.*, vol. 141, pp. 86–99, Jul. 2018.

[7] L. Wang, P. D. Groves, and M. K. Ziebart, "Multi-constellation GNSS performance evaluation for urban canyons using large virtual reality city models," *J. Navigat.*, vol. 65, no. 3, pp. 459–476, 2012.

[8] A. Angrisano, "GNSS/INS integration methods," Ph.D. dissertation, Univ. Calgary, Calgary, AB, Canada, 2010.

[9] G. Falco, M. Pini, and G. Marucco, "Loose and tight GNSS/INS integrations: Comparison of performance assessed in real urban scenarios," *Sensors*, vol. 17, no. 2, p. 27, 2017.

[10] S. Godha and M. E. Cannon, "GPS/MEMS INS integrated system for navigation in urban areas," *GPS Solutions*, vol. 11, no. 3, pp. 193–203, Jul. 2007.

[11] K.-W. Chiang, T. T. Duong, and J.-K. Liao, "The performance analysis of a real-time integrated INS/GPS vehicle navigation system with abnormal GPS measurement elimination," *Sensors*, vol. 13, no. 8, pp. 10599–10622, 2013.

[12] W. Wen, X. Bai, Y. C. Kan, and L.-T. Hsu, "Tightly coupled GNSS/INS integration via factor graph and aided by fish-eye camera," *IEEE Trans. Veh. Technol.*, vol. 68, no. 11, pp. 10651–10662, Sep. 2019.

[13] J. Prieto, S. Mazuelas, and M. Z. Win, "Context-aided inertial navigation via belief condensation," *IEEE Trans. Signal Process.*, vol. 64, no. 12, pp. 3250–3261, Jan. 2016.

[14] Q. Xu, X. Li, and C. Y. Chan, "Enhancing localization accuracy of MEMS-INS/GPS/in-vehicle sensors integration during GPS outages," *IEEE Trans. Instrum. Meas.*, vol. 67, no. 8, pp. 1966–1978, Mar. 2018.

[15] G. Zhang and L.-T. Hsu, "Intelligent GNSS/INS integrated navigation system for a commercial UAV flight control system," *Aerosp. Sci. Technol.*, vol. 80, pp. 368–380, Sep. 2018.

[16] P. Xie and M. G. Petovello, "Measuring GNSS multipath distributions in urban canyon environments," *IEEE Trans. Instrum. Meas.*, vol. 64, no. 2, pp. 366–377, Feb. 2015.

[17] Y. Xia, S. Pan, X. Meng, W. Gao, F. Ye, Q. Zhao, and X. Zhao, "Anomaly detection for urban vehicle GNSS observation with a hybrid machine learning system," *Remote Sens.*, vol. 12, no. 6, p. 971, 2020.

[18] G. Zhang, W. Wen, B. Xu, and L.-T. Hsu, "Extending shadow matching to tightly-coupled GNSS/INS integration system," *IEEE Trans. Veh. Technol.*, vol. 69, no. 5, pp. 4979–4991, May 2020.

[19] D. Odijk and P. J. G. Teunissen, "Characterization of between-receiver GPS-galileo inter-system biases and their effect on mixed ambiguity resolution," *GPS Solutions*, vol. 17, no. 4, pp. 521–533, Oct. 2013.

[20] W. Gao, C. Gao, S. Pan, X. Meng, and Y. Xia, "Inter-system differencing between GPS and BDS for medium-baseline RTK positioning," *Remote Sens.*, vol. 9, no. 9, p. 948, Sep. 2017.

[21] J. Paziewski, R. Sieradzki, and P. Wielgosz, "Selected properties of GPS and galileo-IOV receiver intersystem biases in multi-GNSS data processing," *Meas. Sci. Technol.*, vol. 26, no. 9, Sep. 2015, Art. no. 095008.

[22] D. Odijk, N. Nadarajah, S. Zaminpardaz, and P. J. G. Teunissen, "GPS, galileo, QZSS and IRNSS differential ISBs: Estimation and application," *GPS Solutions*, vol. 21, no. 2, pp. 439–450, Apr. 2017.

[23] H. Liu, B. Shu, L. Xu, C. Qian, R. Zhang, and M. Zhang, "Accounting for inter-system bias in DGNSS positioning with GPS/GLONASS/BDS/Galileo," *J. Navigat.*, vol. 70, no. 4, pp. 686–698, Jul. 2017.

[24] Y. Tian, M. Ge, F. Neitzel, and J. Zhu, "Particle filter-based estimation of inter-system phase bias for real-time integer ambiguity resolution," *GPS Solutions*, vol. 21, no. 3, pp. 949–961, Jul. 2017.

[25] R. Odolinski, P. J. G. Teunissen, and D. Odijk, "Combined BDS, galileo, QZSS and GPS single-frequency RTK," *GPS Solutions*, vol. 19, no. 1, pp. 151–163, Jan. 2015.

[26] J. Paziewski and P. Wielgosz, "Accounting for Galileo-GPS inter-system biases in precise satellite positioning," *J. Geodesy*, vol. 89, no. 1, pp. 81–93, 2015.

[27] Y. Lou, X. Gong, S. Gu, and F. Zheng, "An algorithm and results analysis for GPS+ BDS inter-system mix double-difference RTK," *J. Geodesy Geodyn.*, vol. 36, no. 1, pp. 1–5, 2016.

[28] W. Gao, C. Gao, S. Pan, D. Wang, and J. Deng, "Improving ambiguity resolution for medium baselines using combined GPS and BDS dual/triple-frequency observations," *Sensors*, vol. 15, no. 11, pp. 27525–27542, 2015.

[29] Y. Feng, "GNSS three carrier ambiguity resolution using ionosphere-reduced virtual signals," *J. Geodesy*, vol. 82, no. 12, pp. 847–862, 2008.

[30] D. Wang, X. Meng, C. Gao, S. Pan, and Q. Chen, "Multipath extraction and mitigation for bridge deformation monitoring using a single-difference model," *Adv. Space Res.*, vol. 60, no. 12, pp. 2882–2895, Dec. 2017.

[31] W. Gao, C. Gao, and S. Pan, "Single-epoch navigation performance with real BDS triple-frequency pseudorange and EWL/WL observations," *J. Navigat.*, vol. 69, no. 6, pp. 1293–1309, Nov. 2016.

[32] B. Li, "Review of triple-frequency GNSS: Ambiguity resolution, benefits and challenges," *J. Global Positioning Syst.*, vol. 16, no. 1, Dec. 2018.

[33] W. Gao, C. Gao, S. Pan, G. Yu, and H. Hu, "Method and assessment of BDS triple-frequency ambiguity resolution for long-baseline network RTK," *Adv. Space Res.*, vol. 60, no. 12, pp. 2520–2532, Dec. 2017.

[34] H. Wen, S. Pan, W. Gao, and Q. Zhao, "A tightly combined BDS and GPS method for RTK positioning with triple-frequency widelane combinations," in *Proc. China Satell. Navigat. Conf.*, 2019, pp. 49–61.

[35] P. Teunissen, P. Joosten, and C. Tiberius, "A comparison of TCAR, CIR and LAMBDA GNSS ambiguity resolution," in *Proc. 15th Int. Tech. Meeting Satell. Division Inst. Navigat.*, 2003, pp. 2799–2808.

[36] J. Jung, P. Enge, and B. Pervan, "Optimization of cascade integer resolution with three civil GPS frequencies," in *Proc. ION GPS*, Salt Lake City, UT, USA, 2000, pp. 2191–2200.

[37] F. Zhou, D. Dong, P. Li, X. Li, and H. Schuh, "Influence of stochastic modeling for inter-system biases on multi-GNSS undifferenced and uncombined precise point positioning," *GPS Solutions*, vol. 23, no. 3, p. 59, Jul. 2019.

[38] I. Arasaratnam and S. Haykin, "Cubature Kalman filters," *IEEE Trans. Autom. Control*, vol. 54, no. 6, pp. 1254–1269, Jun. 2009.

[39] P. D. Groves, "Shadow matching: A new GNSS positioning technique for urban canyons," *J. Navigat.*, vol. 64, no. 3, pp. 417–430, Jul. 2011.

[40] L. Wang, P. D. Groves, and M. K. Ziebart, "Smartphone shadow matching for better cross-street GNSS positioning in urban environments," *J. Navigat.*, vol. 68, no. 3, pp. 411–433, May 2015.

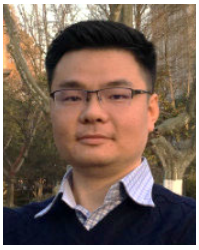

FEI YE received the M.Sc. degree from Hochschule Darmstadt, Germany, in 2011. He is currently pursuing the Ph.D. degree with the School of Instrument Science and Engineering, Southeast University, Nanjing, China. His current research interest includes vehicular applied GNSS/INS integrated positioning in complex urban environments.

SHUGUO PAN received the Ph.D. degree from Southeast University, Nanjing, China, in 2007. He is currently a Professor of Navigation, Guidance, and Control with Southeast University. His current research interests include multi-GNSS/INS combined precise positioning and navigation, and quality control of GNSS positioning.

WANG GAO received the Ph.D. degree from the School of Transportation, Southeast University, Nanjing, China, in 2018. He is currently a Lecturer with Southeast University. His current research interests include multi-system and multi-frequency GNSS integer ambiguity resolution and high-precision positioning.

HAO WANG received the M.Sc. degree from the China University of Mining and Technology, in 2015. He is currently pursuing the Ph.D. degree with the School of Instrument Science and Engineering, Southeast University, Nanjing, China. His current research interests include cycle slip detect and repair of GNSS/INS integrated positioning.

GUOLIANG LIU received the M.Sc. degree from Jiangsu Ocean University, China, in 2019. He is currently pursuing the Ph.D. degree with the School of Instrument Science and Engineering, Southeast University, Nanjing, China. His current research interest includes GNSS/INS/Vision integrated dynamic positioning.

CHUN MA received the M.Sc. degree from the China University of Mining and Technology, in 2020. He is currently pursuing the Ph.D. degree with the School of Instrument Science and Engineering, Southeast University, Nanjing, China. His current research interest include fusion algorithm of GNSS/INS integrated positioning.

YUNFENG WANG received the B.Sc. degree from the Wuhan University of Technology, China, in 2018. He is currently pursuing the master's degree with the School of Instrument Science and Engineering, Southeast University, Nanjing, China. His current research interest includes embedded GNSS/INS integrated positioning.